Research Square

Preprints are preliminary reports that have not undergone peer review.
They should not be considered conclusive, used to inform clinical practice,
or referenced by the media as validated information.

# Evidence for origins of soot emissions from the Chicxulub asteroid impact at the Cretaceous--Paleogene boundary

**Shixiong Hu**

shixiong.hu@uconn.edu

University of Connecticut https://orcid.org/0009-0006-4382-5186

**Clay Tabor**

University of Connecticut https://orcid.org/0000-0002-9915-6157

**Charles Bardeen**

**Owen Toon**

**Wendy Wolbach**

**Joshua Coupe**

Rutgers, The State University of New Jersey https://orcid.org/0000-0002-8652-9970

**Cheryl Harrison**

**Nicole Lovenduski**

University of Colorado Boulder https://orcid.org/0000-0001-5893-1009

**Kenneth MacLeod**

University of Missouri https://orcid.org/0000-0002-6016-0837

**Paul Markwick**

**Siddhartha Mitra**

**Julio Sepulveda**

INSTAAR, University of Colorado, Boulder https://orcid.org/0000-0002-8251-6937

**Robert Kelleher**

**Rachel Wheatley**

**Article**

**Keywords:** Chicxulub impact, Cretaceous–Paleogene boundary, soot, wildfire, CESM, carbon deposition

**Posted Date:** November 3rd, 2026

**DOI:** https://doi.org/10.21203/rs.3.rs-11366946/v1

**License:** This work is licensed under a Creative Commons Attribution 4.0 International License.
Read Full License

**Additional Declarations:** There is **NO** Competing Interest.

# Evidence for origins of soot emissions from the Chicxulub asteroid impact at the Cretaceous–Paleogene boundary

Shixiong Hu[1*], Clay R. Tabor[1], Charles G. Bardeen[2], Owen B. Toon[3], Wendy S. Wolbach[4], Joshua Coupe[6], Cheryl S. Harrison[7], Nicole S. Lovenduski[6], Kenneth G. MacLeod[5], Paul J. Markwick[9], Siddhartha Mitra[10], Julio Sepúlveda[6], Robert Kelleher[6], Rachel Wheatley[8]

[1]Department of Earth Sciences, University of Connecticut, Storrs, Connecticut, 06269, USA.
[2]Atmospheric Chemistry, Observations, and Modeling Laboratory, National Center for Atmospheric Research, Boulder, Colorado, 80301, USA.
[3]Department of Atmospheric and Oceanic Sciences and Laboratory for Atmospheric and Space Physics, University of Colorado Boulder, Boulder, Colorado, 80303-7814, USA.
[4]Department of Chemistry and Biochemistry, College of Science and Health, DePaul University, Chicago, Illinois, USA.
[5]Department of Geological Sciences, University of Missouri, Columbia, Missouri, USA.
[6]Department of Atmospheric and Oceanic Sciences and Institute of Arctic and Alpine Research, University of Colorado Boulder, Boulder, Colorado, USA.
[7]Department of Oceanography and Coastal Sciences and Center for Computation and Technology, Louisiana State University, Baton Rouge, Louisiana, USA.
[8]Department of Geological Sciences, East Carolina University, Greenville, North Carolina, USA.
[9]Knowing Earth Limited, Otley, LS21 3JP, United Kingdom.
[10]Virginia Institute of Marine Science, Gloucester Point, VA 23062, USA.

*Corresponding author(s). E-mail(s): shixiong.hu@uconn.edu;

**Abstract**

Carbon particles released by the Chicxulub asteroid impact may have driven climatic changes and extinction across the Cretaceous-Paleogene (K–Pg) boundary. Geologic support for this possibility comes from globally distributed, carbon-rich deposits at K–Pg boundary sites, but whether this carbon originated from near-global wildfires, impact-site combustion, or both remains debated. Here, we simulate K–Pg carbon-emission scenarios with a state-of-the-art Earth system model and compare modeled carbon deposition with geologic records at K–Pg boundary sites. The simulations show that soot from impact-site combustion alone can produce severe cooling and darkness comparable to near-global wildfire scenarios. However, geological records of carbon deposition at K–Pg sites are more consistent with modeled carbon deposition in simulations that include near-global wildfire emissions. Thus, results suggest that soot derived largely from widespread wildfires was likely a primary driver of end-Cretaceous mass extinction.

**Keywords:** Chicxulub impact, Cretaceous–Paleogene boundary, soot, wildfire, CESM, carbon deposition

# 1 Introduction

The Chicxulub asteroid impact is widely believed to be the cause of the Cretaceous-Paleogene (K–Pg) mass extinction [1–3]. However, the primary kill mechanism(s) remains debated. One potential kill mechanism is reduced sunlight transmission and resulting global cooling due to suspended soot particles, a hypothesis consistent with anomalously high soot concentrations within the iridium-rich K–Pg boundary layer clay [4]. Modeling studies agree that soot could have played a central role in the climate responses and extinction across the K–Pg boundary by absorbing shortwave radiation, leading to surface darkness and cooling [5–7]. Previous studies, though, did not explore the climatic consequences of different potential soot sources, let alone consider which soot sources are most consistent with K–Pg sedimentary records.

The source(s) of soot found in K–Pg boundary sediments is controversial. Based on geologic evidence, Wolbach, Gilmour, and Anders [4] argued that the soot originated from near-global wildfires. In support of this idea, Melosh et al. [8] used modeling to show that global wildfires could have been ignited by an infrared pulse due to the reentry of material from the impactor and impact site. Subsequent ballistic-ejecta modeling suggested a widespread but spatially heterogeneous pattern of wildfires, with wildfires likely near the impact site and its antipode, but the distribution elsewhere dependent on the trajectory of the projectile and angle of impact [9]. Similarly, the modeling work of Morgan, Artemieva, and Goldin [10] showed that infrared radiation from the reentry of ejecta after impact could start wildfires, but their distribution was more likely to occur in distal locations. Furthermore, a follow-up on [8] found that self-shielding of the reentry spherules may have made widespread ignition of wildfires

unlikely [11]. However, more recently Johnson et al. [12], using a similar model, found that the abundant fine dust condensed from rock vapor could promote radiative flux at the surface, making ignition of widespread wildfires more likely.

Studies that examined charcoal records from across North America contended that the deposits at the K–Pg boundary do not support widespread, impact-induced wildfires. They noted that the boundary deposits lack the charcoal signal expected from extensive wildfires [13, 14]. Additional geochemical evidence suggested that the combustion of fossil organic matter and hydrocarbons was necessary to explain the soot and polycyclic aromatic hydrocarbons present in the boundary layer[15, 16]. This interpretation that combustion of fossil organic carbon in the target rocks was a significant source of soot in K–Pg deposits was challenged by Robertson et al. [17], who contended that the previous work had failed to properly adjust for sedimentation rates, and when corrected, the data show that charcoal was present at concentrations expected from global wildfires. Robertson et al. [17] also suggested that the mass of soot coming from the impact site could not account for the amount found in the sedimentary records. More recently, Lyons et al. [18] proposed a release of soot from the impact site followed by wildfires. Their upper limit for the mass injection of soot from the impact site is 17% of the total soot estimated from Wolbach's data [6]. Finally, a new review article, concluded that most of the soot was likely emitted at the time of the impact or shortly thereafter from wildfires [19].

Key uncertainties remain regarding K–Pg soot emissions, and this uncertainty adds complexity to interpretations of both their origin and climatic effects. For example, the vertical distribution and the amount of soot and charcoal produced by wildfires are poorly constrained and may be strongly influenced atmospheric transport and deposition [20]; pyrocumulus can directly inject smoke into the stratosphere [21], whereas weaker wildfires under strong winds may confine emissions to lower atmospheric levels [22]. Here, we use an Earth system model to investigate uncertainties associated with soot emission and its climate effects at the K–Pg boundary.

# 2 Results

## 2.1 Carbon Emission Scenarios

We performed seven soot emission experiments, including wildfire-only, impact-site-only, and combined source scenarios (Table 1). All simulations emit some combination of soot and charcoal from wildfire and/or impact sources, with wildfire emissions released at the surface or tropopause and impact-source emissions released at 50 km altitude. Total carbon emission includes 15 petagrams (Pg) of soot and 41 Pg of charcoal based on studies by Wolbach et al. [4] and the compilation by Bardeen et al. [6]. Here, soot refers to submicron, fractal chain aggregates of elemental carbon monomers and charcoal refers to larger supermicron carbon particles that are not chain aggregates. Soot particles are small and can stay in the atmosphere for years, resulting in significant climate perturbation. In contrast, charcoal particles are relatively large and deposit within weeks, indicating a more local source. As a result, the climatic responses to charcoal are negligible but their deposition is vital for interpreting the sedimentary records at the K–Pg boundary. Below, total carbon refers to the total elemental carbon

preserved in the boundary clay, defined as the sum of soot and charcoal, and the soot fraction is the mass fraction of soot relative to total carbon (see Methods for additional details).

**Table 1** Summary of model simulations.

| Case Name | Fire Soot Pg | Fire Charcoal Pg | Fire Soot Altitude | Fire Charcoal Altitude | Impact Soot Pg | Impact Charcoal Pg | Impact Soot Altitude | Impact Charcoal Altitude |
|---|---|---|---|---|---|---|---|---|
| Fire-56 | 15 | 41 | trop | trop | 0 | 0 | – | – |
| Fire-Surface-56 | 15 | 41 | trop | ground | 0 | 0 | – | – |
| Impact-56 | 0 | 0 | 0 | 0 | 15 | 41 | Strato | Strato |
| Impact-2.5 | 0 | 0 | 0 | 0 | 2.5 | 0 | Strato | – |
| Impact-0.75 | 0 | 0 | 0 | 0 | 0.75 | 0 | Strato | – |
| Fire-Impact-56/2.5 | 12.5 | 41 | trop | trop | 2.5 | 0 | Strato | – |
| Fire-Impact-56/1.6 | 12.5 | 41 | trop | trop | 1.625 | 0 | Strato | – |

Pg denotes petagrams; Trop denotes tropopause; and Strato denotes stratopause.

## 2.2 Simulated Climate Responses

Soot emission from the Chicxulub asteroid impact leads to extreme changes in surface light, temperature, and precipitation that last for more than a decade. Here, we compare the first decade of climate responses from four emission scenarios: Fire-56, Impact-0.75, Impact-2.5, and Fire-Impact-56/1.6 (Table 1 1). Despite substantial differences in the source of soot and the magnitude of emission, three emission scenarios (Fire-56, Fire-Impact-56/1.6, and Impact-2.5) produce similar global climate perturbations, including initial surface light reduction of over 99%, maximum surface cooling of ∼15 °C, and maximum precipitation loss of over 80% (Fig. 1; Supplementary Figs. 1–3). Furthermore, although Impact-0.75 only emits 5% as much soot as the best estimate from the Wolbach records, the global surface temperature and precipitation responses are comparable in magnitude to Fire-56 and Fire-Impact-56/1.6 (Fig. 1). However, regionally, Impact-0.75 produces a bit less cooling over land, primarily in the high latitudes, which is offset globally by slightly greater cooling over much of the ocean. In addition, regarding the extent and duration of the darkness caused by the soot among simulations, Impact-0.75 produces by far the fewest months with light below the threshold for photosynthesis (1% of the pre-impact climate based on [23]), with less than 18 months at the poles and low latitudes (Fig. 1). In contrast, Fire-56 and Impact-2.5 show strong spatial similarity, with most locations reaching 18-30 months with light below 1% of the control. Fire-Impact-56/1.6 produces the most extensive and persistent low-light response, with mid- and low-latitudes experiencing 24-36 months of light below 1%. Although there are some differences between emission scenarios with regard to the ability to photosynthesize, they do not translate into large temperature and precipitation differences because the overall magnitude of surface shortwave energy reduction is similar (Fig. 1).

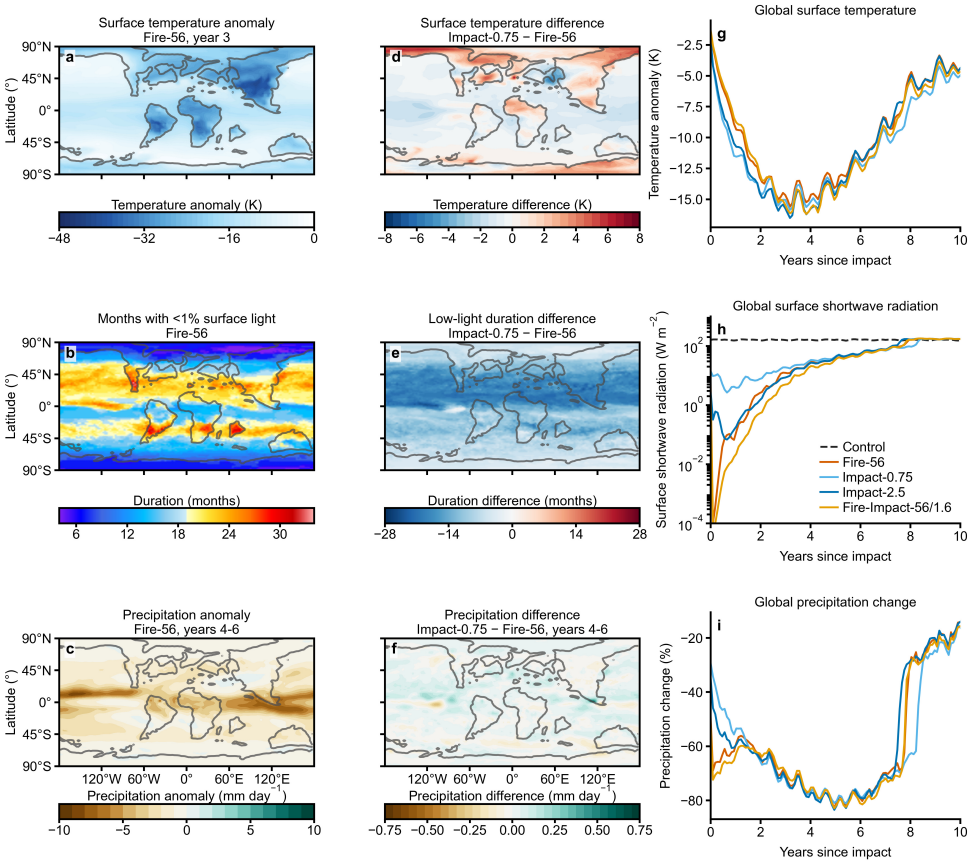



**Fig. 1 Climate response to soot-emission scenarios.** Panels a–c show the Fire-56 mean surface-temperature anomaly of year 3 (K), cumulative months during the nine years after impact with downwelling surface shortwave radiation below 1% of the control, and mean precipitation anomaly of years 4–6 (mm day$^{-1}$). Note, surface shortwave radiation below 1% of the control is used as the threshold for photosynthesis based on the work of Morel et al., (1988) [23], who defined the euphotic depth using 1% of surface downwelling solar flux. Panels d–f show Impact-0.75 minus Fire-56 for the same variables as a–c. Panels g–i show global-mean surface-temperature anomaly (K), downwelling surface shortwave radiation (W m$^{-2}$; logarithmic scale), and precipitation change relative to the control (%).

The timing of surface light, temperature, and precipitation recovery among all simulations is similar (panel g, h, and i in Fig. 1). Nine years after impact, the global surface temperature anomaly remains approximately 5 °C below the control values, and the precipitation is about 20% less than the control in all four emission scenarios (panel g, h, and i in Fig. 1). In contrast, surface shortwave radiation recovers relatively rapidly in all emission scenarios, returning to control levels approximately 7 years after the impact. This abrupt recovery of surface light is the result of saturation of the atmospheric column and rapid removal of soot due to scavenging [6].

## 2.3 Carbon Deposition Comparison

We evaluate the plausibility of simulated carbon deposition by comparing the sedimentary records of Wolbach et al. [4] with four emission scenarios: Fire-56, Fire-Surface-56, Impact-56, and Fire-Impact-56/2.5. Among these scenarios, Fire-Surface-56 produces the strongest localized charcoal deposition signal because charcoal is only emitted in the boundary layer, not at the tropopause (panel d, h, and l in Fig. 2). As a result, charcoal is deposited soon after its formation in regions adjacent to the fire sources (Fig. 2). Consequently, charcoal deposition and total carbon deposition, which is dominated by charcoal, are more than twice as large as in the other emission scenarios across low- and mid-latitude regions.

Carbon deposition in Fire-Impact-56/2.5 (panel c, g, and k in Fig. 2) broadly resembles Fire-56 (panel a, e, and i in Fig. 2), which is expected because only 17% of soot comes from the impact site in Fire-Impact-56/2.5. Total carbon deposition maxima occur at high latitudes and equatorial continents, reflecting the vegetation carbon used to estimate the magnitude and spatial distribution of the wildfire emissions (Supplementary Fig. 4). The subtle differences in carbon deposition between Fire-Impact-56/2.5 and Fire-56 might be a result of the longer atmospheric residence time of impact-site soot in Fire-Impact-56/2.5.

Impact-56 shows a pronounced divergence from the other emission scenarios in terms of the geospatial pattern of soot and charcoal deposition. As expected, emission of charcoal near the stratopause instead of at the tropopause extends its atmospheric residence time and allows transport over greater distances. However, the resulting geospatial pattern of charcoal deposition is not globally uniform; instead, it is concentrated primarily at mid- to high-latitudes associated with transport by the brewer-dobson circulation (panel j in Fig. 2). Similarly, soot emitted in Impact-56 is deposited mainly over high-latitude oceans.

Model-proxy agreement varies between sites and is better constrained for total carbon deposition than for soot fraction (Figure 3). In terms of total carbon deposition, the modeled range is in agreement with the records at New Zealand, Caravaca, and Stevns Klint. At New Zealand, most emission scenarios fall within or close to the uncertainty range, although their upper bound is 12 mg $cm^{-2}$, which is slightly below the proxy central value of about 14 mg $cm^{-2}$. At Caravaca, the Fire-56 and Fire-Impact-56/2.5 cases are the closest scenarios to the record, largely overlapping between 6-10 mg $cm^{-2}$. At Stevns Klint, the modeled spread is large, but several emission scenarios fall within the range of the record.

Across all sites, the discrepancies in the simulated soot fraction between emission scenarios are statistically indistinguishable, and the missing error bars make direct comparison more challenging. At Stevns Klint, Impact-56 is centered closest to the soot fraction of 0.21. Fire-56 and Fire-Impact-56/2.5 over predict the records, while the broader Fire-Surface-56 distribution spans the record. The agreement in soot faction between the emission scenarios and the sedimentary records is closest at Gubbio and El Kef, whereas the simulations overestimate the soot fraction at Sumbar.

Wildfire emission scenarios better correlate with the Wolbach total carbon deposition records than the impact-only scenario. In order to account for the uncertainty in the sedimentary records, the differences between the model and geologic data were weighted

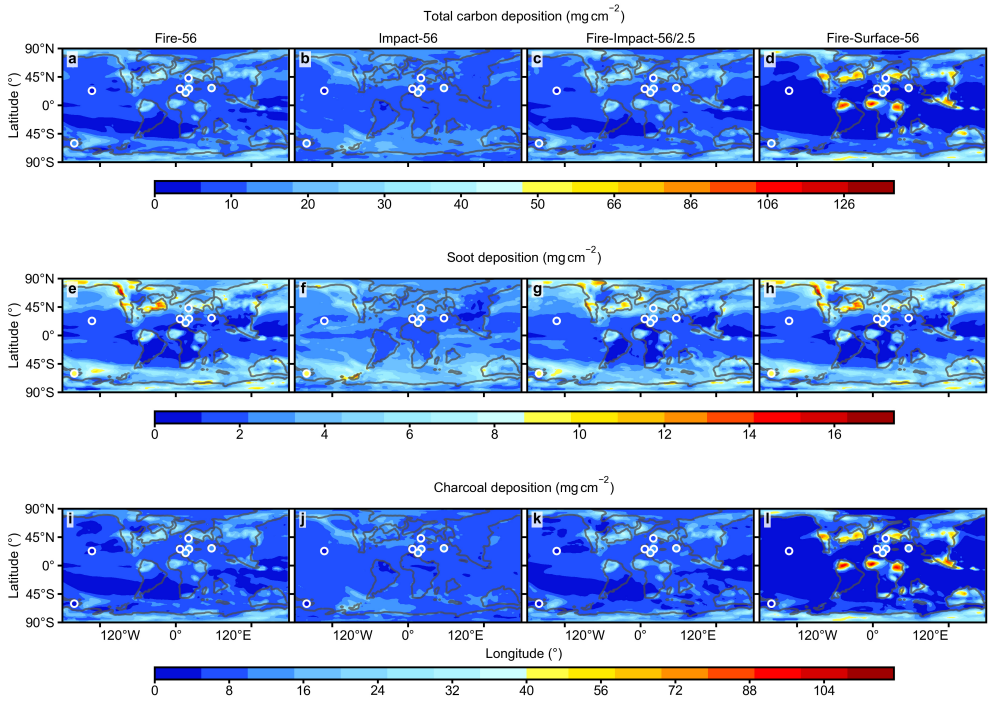



**Fig. 2 Spatial patterns of modeled carbon deposition.** Rows show total carbon (a–d), soot (e–h) and charcoal (i–l) deposition in mg cm$^{-2}$. Columns show Fire-56 (a, e, i), Impact-56 (b, f, j), Fire-Impact-56/2.5 (c, g, k) and Fire-Surface-56 (d, h, l). Open white circles mark the Wolbach boundary sites used for comparison [4].

**Table 2** Model–proxy misfit metrics for total carbon deposition and soot fraction.

| Case | Total carbon (%) | | | Soot fraction (%) | | |
|---|---|---|---|---|---|---|
| | RMSE | Bias | Error | RMSE | Bias | Error |
| Fire-56 | 38.0 (33.7) | -17.0 (2.1) | 34.0 (33.6) | 60.5 | -18.9 | 57.5 |
| Impact-56 | 45.1 (52.0) | -20.3 (15.9) | 40.3 (49.5) | 55.0 | -18.0 | 52.0 |
| Fire-Impact-56/2.5 | 36.2 (35.6) | -17.2 (8.4) | 31.9 (34.6) | 58.8 | -11.1 | 57.7 |
| Fire-Surface-56 | 58.6 (41.8) | -31.4 (-23.0) | 49.4 (35.0) | 52.7 | 8.3 | 52.0 |

Metrics are expressed as percentages of the corresponding mean Wolbach value across the seven sites: 11.327 mg cm$^{-2}$ for total carbon deposition and 0.286 for soot fraction. Calculations use unrounded means. RMSE denotes root mean squared error; error denotes centered residual scatter after removing the mean bias. Total-carbon entries give unweighted values and uncertainty-weighted values in parentheses. Soot-fraction metrics are unweighted because proxy uncertainty estimates are unavailable. Weight definitions are provided in Supplementary Methods.

by the selected asymmetric uncertainty widths. Both unweighted and weighted (in parentheses in Table 2) total-carbon metrics indicate that the wildfire-related emission scenarios, except for Fire-Surface-56 in the unweighted result, reproduce the Wolbach

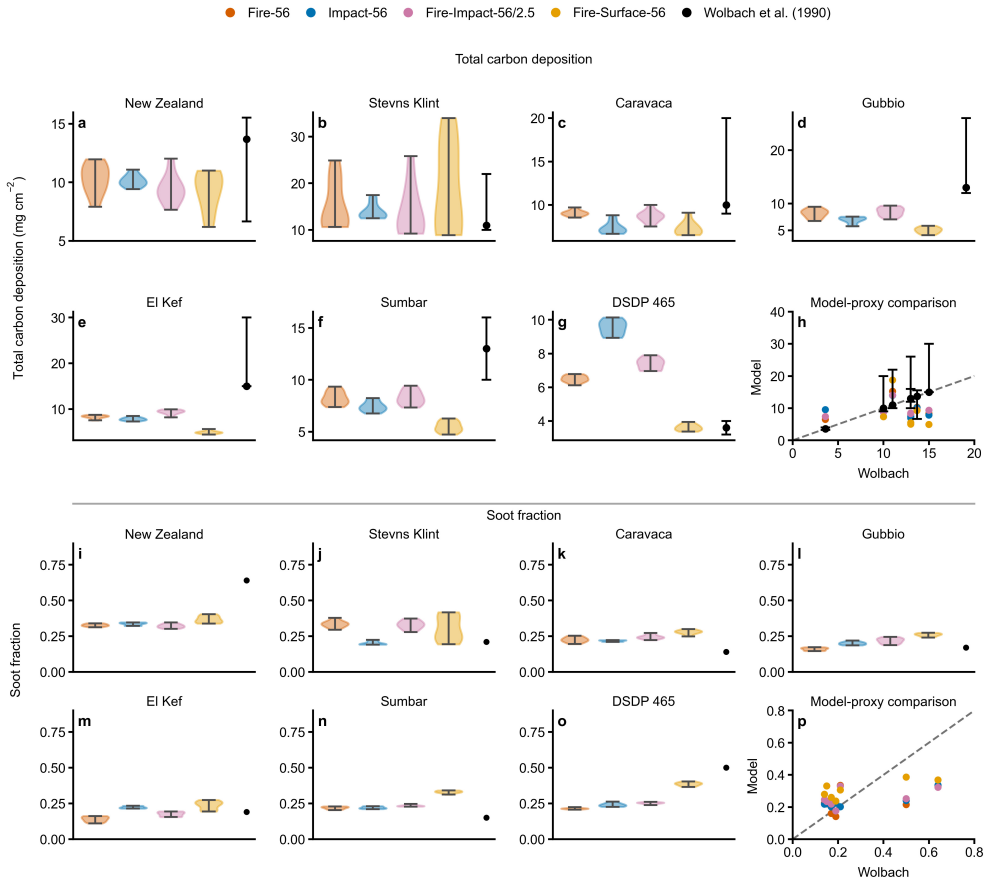



**Fig. 3 Model–proxy comparison across seven K–Pg boundary sites.** Panels a–g show total-carbon deposition (mg cm$^{-2}$), and panels i–o show soot fraction, for Fire-56 (red), Impact-56 (blue), Fire-Impact-56/2.5 (purple) and Fire-Surface-56 (yellow). Violin distributions contain the central model grid cell at each site and its eight adjacent cells; black points show Wolbach central values [4]. Total-carbon error bars are the reported asymmetric measurement uncertainties; proxy uncertainty is unavailable for soot fraction. Panels h and p compare each simulated grid-cell value with the corresponding proxy value; dashed lines show 1:1 agreement. WACCM/CARMA denotes the coupled Whole Atmosphere Community Climate Model–Community Aerosol and Radiation Model for Atmosphere simulation; DSDP denotes the Deep Sea Drilling Project.

deposition record better than Impact-56 (Supplementary Methods; Supplementary Table 1). For unweighted results, Fire-Impact-56/2.5 has the lowest total carbon deposition RMSE and error, closely followed by Fire-56. In comparison, Impact-56 has a larger total carbon deposition RMSE and a more negative bias along with a larger error. Fire-Surface-56 performs the worst for unweighted total carbon, mainly due to mismatch at several shallow coastal sites. For the more robust weighted comparisons, all fire emission scenarios perform better than Impact-56. Here, Fire-56 has the lowest

RMSE, followed by Fire-Impact-56/2.5, Fire-Surface-56, and Impact-56. Regardless of metric, Fire-56 and Fire-Impact-56/2.5 clearly perform the best.

Soot fraction differentiates the emission scenarios less clearly than total carbon deposition despite overall lower normalized RMSEs. Fire-Surface-56 has the smallest soot fraction RMSE, followed by Impact-56, Fire-Impact-56/2.5, and Fire-56. However, the lack of error bars for soot fraction greatly limits the interpretation of uncertainties, and the RMSE differences between simulations are minimal relative to total carbon. Likewise, both the biases and the errors of the soot fraction comparisons fall in a smaller envelope compared to total carbon deposition.

We also calculated the normalized error and bias for total carbon deposition and soot fraction, allowing the two metrics to be directly compared (Supplementary Table 2). We find that soot fraction has lower normalized RMSE than total carbon deposition in all cases (0.753–0.865 versus 1.083–1.750), indicating smaller residuals relative to the spread of the records. However, the soot fraction remains tightly clustered, whereas total carbon deposition gives stronger scenario separation, with Fire-Impact-56/2.5 and Fire-56 greatly outperforming Impact-56 and Fire-Surface-56.

The soot and charcoal deposition data compiled from the Wolbach records [4] and from each emission scenario show varying correlations with distance from the Chicxulub impact crater and distance from vegetation (Figs. 4 and 5). Soot deposition (Fig. 4, panels a, c, e and g), for the sedimentary records and all simulated cases, is weakly correlated with distance from the crater. However, wildfire emission simulations show modest negative correlations between soot and distance to nearest vegetation with a fuel load greater than 2.0 g C $cm^{-2}$ whereas soot from sedimentary records is essentially uncorrelated with vegetation distance (a value typical of modern tropical forests is 1.45 $\pm$ 0.5 g C $cm^{-2}$; [24]). In the wildfire emission simulations, charcoal deposition increases with distance from the crater. The Wolbach data similarly show that the deposition of charcoal increases with distance from the crater (Fig. 5, panel d). Charcoal from sedimentary records also has a strong negative relationship with vegetation distance (R = -0.74; Fig. 5, panels a and b). Charcoal deposition in the wildfire cases is also negatively correlated with distance to the nearest vegetation, with the strongest relationship in Fire-56. In contrast, in the Impact-56 case, charcoal is only weakly correlated with distance from the crater or vegetation.

# 3 Discussion

## 3.1 Climate Responses

Our simulations show that impact-generated soot alone can reproduce the severity of the post-impact climate perturbation, even when the total carbon burden is much smaller than the values measured by Wolbach et al. [4]. Both Impact-2.5 and Impact-0.75 produce spatial and temporal patterns of cooling and precipitation reduction like those in the near-global wildfire emission scenarios (Fig. 1; Supplementary Figs. 1–3). Particularly, Impact-0.75, which only emits 0.75 Pg of soot, still prevents 90% of the light from reaching the surface during the first year after impact, causes a maximum global mean surface cooling of 15°C, and a reduction in total precipitation by more than

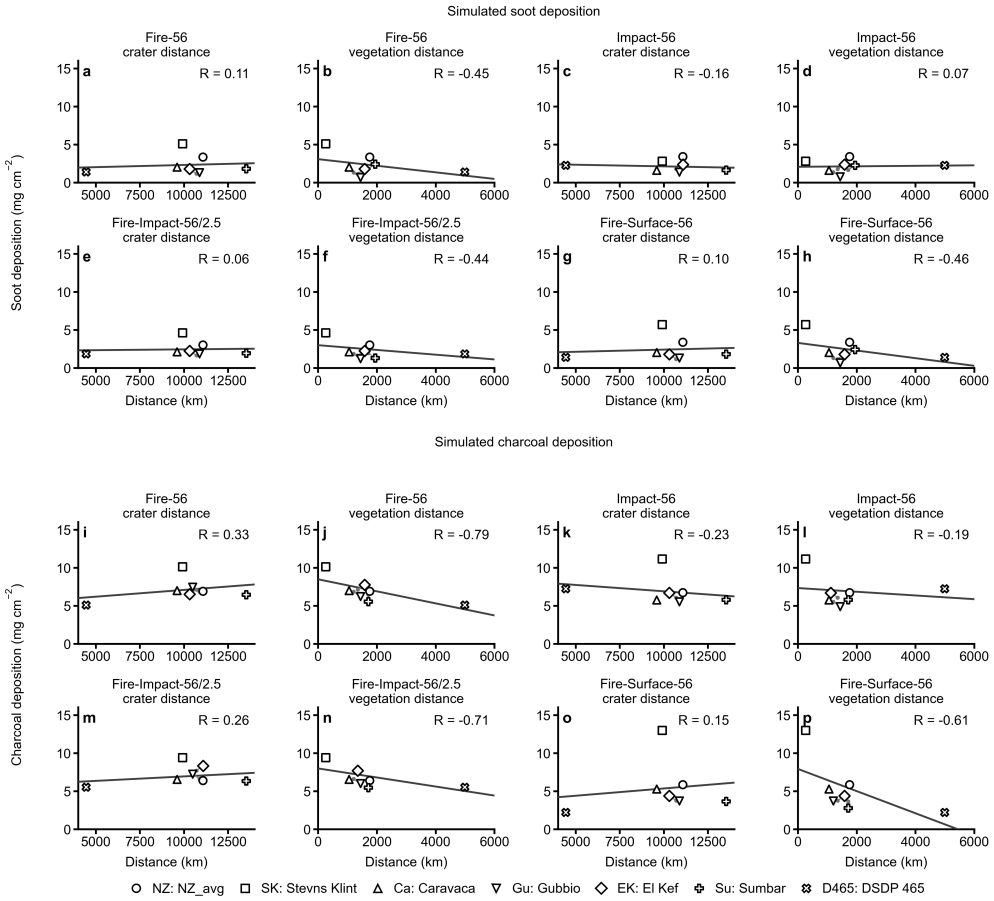



**Fig. 4 Relationships between simulated deposition and source distance.** Panels a–h show simulated soot deposition and panels i–p show simulated charcoal deposition (mg cm$^{-2}$). Within each deposition block, adjacent panel pairs show Fire-56 (a, b; i, j), Impact-56 (c, d; k, l), Fire-Impact-56/2.5 (e, f; m, n) and Fire-Surface-56 (g, h; o, p). Odd-numbered panels (a,c,e,g,i,k,m,o) use distance from the Chicxulub crater; even-numbered panels (b,d,f,h,j,l,n,p) use distance to the nearest vegetation grid cell with biomass fuel above 2.0 g C cm$^{-2}$. Points denote the seven comparison sites, lines are ordinary least-squares fits, and R is the Pearson correlation coefficient; distances are km. DSDP 465 denotes Deep Sea Drilling Project Site 465; NZ_avg is the mean of the Woodside Creek, Chancet Rocks and Flaxbourne River sites in New Zealand.

80% during year 4 after impact. This result suggests that soot is of great importance to the climate response after the K–Pg boundary, even if wildfires did not occur.

While the overall climate responses are similar, simulated emission scenarios differ in the number of months with a surface light level below 1% of normal, which we use as a threshold for the ability of organisms to photosynthesize [23]. Impact-0.75 produces the weakest low-light response (Fig. 1; Supplementary Fig. 2). Its limited cumulative low-light duration indicates that this lower-bound impact-site soot case is unlikely to produce a sustained global shutdown of photosynthesis. If light reduction is

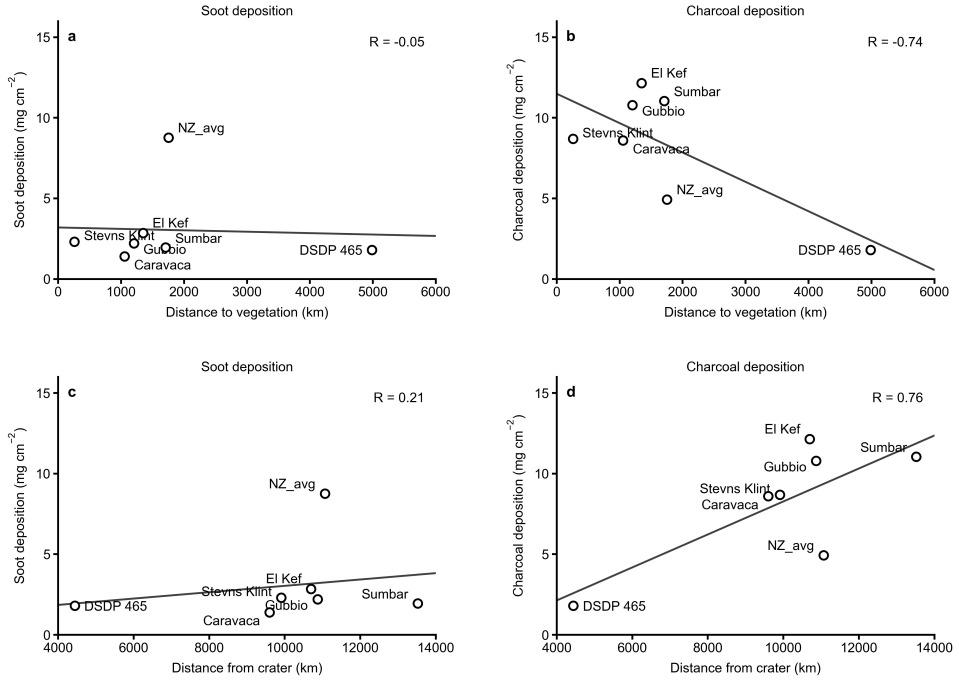



**Fig. 5 Relationships between sedimentary record deposition and source distance.** Wolbach soot (a, c) and charcoal (b, d) deposition [4] (mg cm$^{-2}$) are compared with distance to the nearest vegetation grid cell with biomass fuel above 2.0 g C cm$^{-2}$ (a, b) and distance from the Chicxulub crater (c, d). Points denote the seven comparison sites, lines are ordinary least-squares fits, and R is the Pearson correlation coefficient; distances are km. DSDP 465 denotes Deep Sea Drilling Project Site 465; NZ_avg is the mean of the Woodside Creek, Chancet Rocks and Flaxbourne River sites in New Zealand.

assumed to be the primary kill mechanism, Impact-0.75 would therefore represent the least severe emission scenario relevant to extinction among those examined. Increasing the impact-site soot burden from 0.75 Pg to 2.5 Pg greatly expands the area and duration of low-light conditions, producing patterns broadly comparable to Fire-56 across tropical and subtropical regions. This contrast indicates that within the range of modeled soot input, the magnitude of impact-site soot emissions exerts a strong control on the persistence and spatial extent of post-impact darkness.

Although the magnitude of the soot based on Wolbach et al. [4] requires a significant fraction of the Earth to burn, our results also suggest that there may be a similar post-impact climate response from regional burn scenarios such as those proposed in Morgan, Artemieva, and Goldin [10] and Arinobu et al.[25]. Indeed, Bardeen et al.[6] and Tabor et al.[7] showed that significantly smaller wildfire emission scenarios were still capable of producing a similar climate response. However, simulations of partial burn scenarios would be unlikely to match the geologic records of carbon deposition as well as the global burn scenarios presented here.

### 3.2 Model-Data Comparisons

Regarding the model-data comparison, we find that near-global wildfires are necessary to capture the spatial pattern of measured total carbon deposition; the impact emission scenarios do not produce enough soot nor charcoal, and lead to a poorer spatial distribution of total carbon deposition when compared with the sedimentary records. Although none of our proposed simulations agree exceptionally well with the Wolbach et al. [4] records, especially at low-latitude shallow-marine sites, the overall correspondence between the simulated carbon deposition in our wildfire experiments and the Wolbach records is notable, given the large uncertainties that could influence carbon deposition at the K–Pg boundary. Fire-56 and Fire-Impact-56/2.5 perform best in terms of total carbon deposition, comparing better to the geologic data than Impact-56 across six of the seven sites and five of the seven sites, respectively. In contrast, Fire-Surface-56 performs best when comparing modeled and geologic soot fraction. However, the simulated soot fraction error and bias are quite similar among emission scenarios. Furthermore, the lack of error bars in the soot fraction data makes comparisons challenging, as the clustered biases and errors make it difficult to differentiate each emission scenario.

Looking further into the spatial distributions, we find that simulated soot deposition is not correlated with distance from the Chicxulub impact crater. Simulated soot is also not correlated with distance from vegetation in the impact case and is only weakly correlated with distance from vegetation in the wildfire cases. Similarly, soot from sedimentary records show weak correlation with distance to the impact-site and no correlation with distance from vegetation. This lack of correlation is expected because regardless of the source, soot could be transported for years due to its small particle size. Soot is expected to be globally distributed if it is injected near the troposphere, as has been observed for modern soot from large wildfires [26]. In contrast, simulated charcoal deposition declines with distance from vegetation in the wildfire cases because the charcoal is too large to be carried far by the wind [27]. This relationship also exists in the Wolbach records. Moreover, charcoal content increases with the distance from the crater in both the wildfire cases and the Wolbach records, probably because sites away from the crater tend to be closer to dense vegetation. However, these correlations do not exist in Impact-56. Therefore, the spatial relationships of soot and charcoal deposition found in both model and sedimentary data favor widespread wildfires as the dominant source of the carbon preserved at the K–Pg boundary.

## 4 Limitations

There are several limitations in our study associated with the inherent uncertainties of geological data and modeling constraints. Most of the sample sites are thought to be shallow marine locations at the time of the K–Pg boundary [4, 28], except for Deep Sea Drilling Project (DSDP) Site 465 in the North Pacific. A portion of the carbon deposition at sites near the coast might occur via river runoff and thus might not be entirely from airfall deposition [4]. For instance, the three sites at New Zealand (Woodside Creek, Chancet Rocks, and Flaxbourne River) show significant variation in carbon deposition despite their proximity. In contrast, carbon at DSDP Site 465 is

likely primarily of atmospheric origin, but might be influenced by currents as it settles to the sea floor. While carbon transport by rivers and ocean currents is not simulated by our model, the general agreement between our simulated carbon deposition and a variety of depositional environments lends credence to our conclusions.

We acknowledge that model boundary conditions may impact our model outputs. For instance, we did not adjust our paleogeographic reconstruction to explore the role of sea level during the Maastrichtian, which may have varied by up to 75 m [29]. This adjustment could lead to changes in the shorelines near where most of the records originate, and therefore, the distance between the records and the nearest vegetation. However, we attempted to account for this uncertainty by comparing with the grid cells that surround the paleo-locations of the sample sites. Another uncertain model boundary condition is vegetation, for which we used the Maastrichtian reconstruction from Sewall et al. [30]. Their reconstruction is based on few data points, and large uncertainties in the regional vegetation cover remain, which could affect the emission and deposition of carbon in our simulations. That said, vegetation carbon is simulated by the model, which informs our emission scenarios.

Our simulated emissions simplify the actual emissions associated with the Chicxulub impact. Here, we only included soot, charcoal, and water, as water is the most likely emission to significantly affect the rate of carbon deposition. Other impact emissions, such as dust and sulfate, may have interacted with carbon. However, the different elevations and timing of the carbon emissions from wildfires may have limited interaction with other aerosols. Furthermore, our simulated carbon consists of pure black carbon. Although the impact-triggered wildfires likely differ from modern wildfires in many ways, there was still likely to be some amount of organic coating, which may have influenced deposition [21]. However, the extreme heat from the global wildfires at the K–Pg could potentially consume most of the organics, limiting their effect on atmospheric residence time [31].

# 5 Conclusion

Our model simulations show that impact-only emission scenarios produce similar global surface cooling, darkness, and precipitation reduction to wildfire emission scenarios with significantly more soot emission. However, the minimum soot emission scenario, impact-0.75, is not sufficient to reproduce the persistent near-total darkness seen in other cases, which may have important implications for the extinction of photosynthesizers. Nevertheless, our findings point to an important role for soot in the K–Pg boundary mass extinction regardless of emission source.

By directly comparing our model results with soot and charcoal records, we find that constraining the K–Pg carbon emissions is challenging due to uncertainties in the model boundary conditions and the geologic records. Nevertheless, our modeled total carbon deposition suggest that widespread wildfires at the K–Pg boundary best explain the geologic records. Furthermore, both the sedimentary records and simulated distribution of charcoal, but not soot, decline in proportion with distance from vegetation sources, suggesting a wildfire origin. Together, these findings provide robust support for widespread wildfires soon after the Chicxulub asteroid impact.

# 6 Methods

## 6.1 Model

We utilize the Community Earth System Model Version 2 codebase (CESM2) [32], in a fully coupled model configuration with dynamic atmosphere, ocean, land, sea ice, and river runoff components. For the atmosphere component, we use the Whole Atmosphere Community Climate Model version 4 (WACCM4) [33] paired with the Community Aerosol and Radiation Model for Atmosphere (CARMA) [34]. WACCM4 has 66 levels in the vertical extending into the thermosphere and includes an interactive chemistry module. CARMA is a sectional aerosol model; each aerosol type is tracked using a set of 21 size bins, whose concentrations can evolve freely. Other changes made for model stability are described in Bardeen et al. [6] and Tabor et al. [7]. We also use the Community Land Model version 4 (CLM4) [35] with active carbon and nitrogen cycling, the Parallel Ocean Model version 2 (POP2) [36] with Marine Biogeochemistry Library (MARBL) [37], and the Community Sea Ice Model version 4 (CICE4) [38]. Atmosphere and land have a horizontal resolution of $1.9° \times 2.5°$. Ocean and sea ice have a nominal horizontal resolution of $1°$.

## 6.2 Maastrichtian Boundary Conditon

Topography during the Maastrichtian is an updated version of Markwick and Valdes [39]. The Maastrichtian vegetation comes from Sewall et al. [30] with plant phenology calculated by carbon and nitrogen cycling within CLM4 [35].Specifically, we remapped this reconstruction to our Maastrichtian topography, and the Plant Functional Types (PFTs) from Sewall et al. [30] were converted to CLM4 PFTs. Atmospheric $CO_2$ is 850 ppm to reflect late Maastrichtian geologic estimates [40]. Atmospheric $CH_4$ and $N_2O$ estimates are 2400 ppb and 375 ppb, respectively, and come from model simulations [41]. A reduced solar constant (1357.07 W $m^{-2}$) is applied based on the calculations of Gough [42]. Prescribed aerosols are "paleotized" via preindustrial defaults from CESM with the methods from Tabor et al. [7]. All simulations are initialized from a previously equilibrated Maastrichtian simulation.

## 6.3 Carbon Particle Representation

Here, we use the term soot to refer to submicron, fractal chain aggregates of elemental carbon monomers, typically less than 0.1 $\mu$m in diameter, which have been identified in K–Pg boundary sediments. These aggregate particles are sometimes described as aciniform carbon. Observations from modern wildfires indicate that aggregate soot is predominantly submicron, with a mean diameter of $\sim$0.13 $\mu$m [43], consistent with measurements from K–Pg boundary samples [44]. This similarity suggests modern wildfires are a plausible microphysical analogue for soot produced during the Chicxulub impact event. Due to their small size, such particles have low settling velocities and can be transported over long distances, although coagulation can increase particle size and enhance deposition rates.

We use the term charcoal to denote larger supermicron carbon particles that are not chain aggregates. As characterized by Wolbach, Gilmour, and Anders [4], these particles

consist primarily of combustion-derived plant material, with smaller contributions from detrital carbon and kerogen. In modern wildfire emissions, charcoal represents a second particle size mode, with a mean volume radius of ∼5 $\mu$m [43]. Owing to their larger size, these particles settle more rapidly than soot and are less likely to be transported far from their source; they too may grow through coagulation.

Our estimate of total (sum of soot and charcoal) elemental carbon emission at the K–Pg boundary comes from the study of Bardeen et al. [6]. They estimated 15 petagrams (Pg) of soot and 41 Pg of charcoal from studies by Wolbach et al. [4]. We emit this carbon from both fire and impact-derived sources. For fire emissions, we input soot at the tropopause and charcoal at surface or tropopause following the Gaussian vertical distribution from Toon, Bardeen, and Garcia [20]. The spatial pattern of fire-derived soot emission is based on the fraction of total vegetation carbon within each terrestrial grid cell as simulated by CLM4. Impact-derived soot is considered a ballistic emission and is injected globally, following a Gaussian vertical distribution centered at 50 km [20]. The portion of soot derived from the impact site as noted in Table 1 comes from the estimates in Lyons et al. [18]. All simulations also inject $7.21 \times 10^3$ Pg of water vapor into the atmosphere, following the suggested amount and a source-dependent distribution from Toon, Bardeen, and Garcia [20], as the source of the emission of water vapor in the model is categorized into the wildfires, impact-site, and splashed seawater. Based on the ranges of During et al. [45] and DePalma et al. [46], and the palaeobotanical evidence by Wolfe [47], we inject all emissions on May 1st over 1 day.

Elemental carbon, principally in the form of soot, accounts for 2% of the emitted smoke mass on a mass basis. Representing the soot morphology also requires specifying the particle size distribution and microphysical structures of the carbon particles. Following Bardeen et al. [6], we assume fractal soot particles with a monomer radius of 30 nm. The fractal dimension for soot varies with particle mass from 1.5 to 3.0. The charcoal particles are assumed to be fractal with a lognormal number size distribution having an initial mode radius of 1.85 $\mu$m and sigma of 1.8, which produces a volume mean radius of 5 $\mu$m. For charcoal the fractal dimension we apply is 2.2, and the packing coefficient is 1.0. The default observed mean soot radius value of 0.11 $\mu$m in a lognormal size distribution with a width of 1.6 comes from Wolbach et al. [48].

## 6.4 Experiment design

We performed 7 emission experiments (Table 1) using the state-of-the-art Community Earth System Model (CESM; see Methods) to explore the potential source of soot and charcoal at the K–Pg boundary and their associated climate effects. We run two near-global fire-only emission experiments: 1) Fire-56, which emits 15 Pg of soot and 41 Pg of charcoal at the tropopause, and 2) Fire-Surface-56, which emits 15 Pg of soot at the tropopause and 41 Pg of charcoal at the surface, following the Gaussian vertical distribution in the Eq.2 and 3 from Toon, Bardeen, and Garcia [20] and assuming the local boundary layer is relatively shallow. Soot is injected at tropopause, with its distribution completely falls in eq (2) because the globally distributed soot particles could be lofted by the widespread intense wildfires into the upper troposphere and stratosphere through strong convection. Kalashnikova et al. [49] found that the micrometeorites entering the present-day atmosphere ablate at an altitude of near

85 km, because the micrometeorites stop after encountering air of the same mass. Therefore, the distribution is taken to be Gaussian distribution centered at 70 km. From Toon, Bardeen, and Garcia [20], soot emissions is assumed to be injected at lower altitudes but still using the Gaussian distribution. These simulations explore the potential role of near-global fire soot emissions at the K–Pg boundary and the uncertainty in the elevation reached by charcoal particles. We also run three impact-only soot emission experiments. Impact-2.5 and Impact-0.75 ballistically emit 2.5 Pg and 0.75 Pg of soot, but no charcoal. Impact-2.5 and Impact-0.75 represent the maximum and minimum impact-soot estimates from Lyons et al. [18] and serve to isolate the effects of impact-derived soot on the climate. We also perform Impact-56, in which we ballistically emits 15 Pg of soot and 41 Pg of charcoal, assuming all the carbon originated from the impact site. Finally, we run two combined soot emission experiments. Fire-Impact-56/2.5 includes 2.5 Pg of soot from the impact site at 50 km, 12.5 Pg of soot from near-global wildfires injected at the tropopause, and 41 Pg of charcoal from near-global wildfires injected at the tropopause. Similarly, Fire-Impact-56/1.6 includes 1.625 Pg of soot from the impact site at 50 km, 12.5 Pg of soot from near-global wildfires injected at the tropopause, and 41 Pg of charcoal from near-global wildfires injected at the tropopause.

## 6.5 Geologic Records

We considered soot data from 12 soot deposition sites published by Wolbach et al. [4, 48, 50] including Stevns Klint (Denmark), Gubbio (Italy), Caravaca (Spain), Agost (Spain), Raton (US), Elendgraben (Austria), El Kef (Tunisia), Sumbar (Turkmenistan), Woodside Creek (New Zealand), Chancet Rocks (New Zealand), Flaxbourne River (New Zealand), and DSDP 465 (Pacific Ocean). After vetting, we were left with 7 data sites for comparison with our model results. The record from Agost is not compared with our simulation data due to use of the 600h dichromate etching technique, which may have preferentially destroyed the organic part of the sample. Likewise, data at site Elendgraben are excluded because the $H_2O_2$ treatment may lead to the loss of carbon from the sample. The samples collected at Raton are also not compared with our simulation data due to large amounts of coal at the site, which makes it difficult to identify the fine soot particles. Unlike the other sites, Raton was not a marine site, but a swamp during the Maastrichtian. Finally, we averaged the three sites in New Zealand (Woodside Creek, Chancet Rocks, and Flaxbourne River) since all three are located within the same grid cell in our model simulations. More details on the sample processing procedures are described in Wolbach et al. [4].

## 6.6 Evaluating Modeled Carbon Deposition

We evaluated each simulation by comparing modeled total carbon deposition and soot fraction with the vetted Wolbach records. The model value at each site was the mean of the central model grid cell and its eight adjacent cells. Model–proxy differences were summarized using RMSE, bias, and centered residual scatter. For total carbon deposition, we additionally calculated uncertainty-weighted metrics using the upper or lower Wolbach error width according to the sign of the model–proxy difference.

The selected upper or lower uncertainty deviation was converted to its absolute width, and nonzero widths were assigned relative inverse-square weights. El Kef retains its unweighted site weight of 1/7 when its unavailable lower uncertainty, encoded as zero in the analysis inputs, is selected, since the El Kef from the provided error bar missed the lower bound. Therefore, No uncertainty floor is applied. Weighted total-carbon RMSE, bias, and error keep their deposition units before conversion to percentages. Weighted and unweighted total-carbon metrics were expressed as percentages of the mean Wolbach deposition. Soot-fraction metrics were unweighted and expressed as percentages of the mean proxy soot fraction. Separately, residuals for both variables were normalized by their across-site proxy standard deviations for Supplementary Table 2. Further details are provided in Supplementary Methods.

**Data availability**

The post-processed NetCDF data required to reproduce all main-text and Supplementary figures and tables are available in Zenodo at https://doi.org/10.5281/zenodo.21609619.The deposited record includes figure and table-specific datasets and reproduced outputs. The published proxy records analyzed in this study are identified and cited in the manuscript and repository documentation.

**Code availability**

All registered users can access the CESM/CARMA model through the CESM trunk available at https://www.cesm.ucar.edu.

# References


[1] Chiarenza, A. A. *et al.* Asteroid impact, not volcanism, caused the end-Cretaceous dinosaur extinction. *Proc. Natl Acad. Sci. USA* **117**, 17084–17093 (2020). https://doi.org/10.1073/pnas.2006087117.

[2] Hull, P. M. *et al.* On impact and volcanism across the Cretaceous-Paleogene boundary. *Science* **367**, 266–272 (2020). https://doi.org/10.1126/science.aay5055.

[3] Schulte, P. *et al.* The Chicxulub asteroid impact and mass extinction at the Cretaceous-Paleogene boundary. *Science* **327**, 1214–1218 (2010). https://doi.org/10.1126/science.1177265.

[4] Wolbach, W. S., Gilmour, I. & Anders, E. Major wildfires at the Cretaceous/Tertiary boundary. In *Global Catastrophes in Earth History: An Interdisciplinary Conference on Impacts, Volcanism, and Mass Mortality* (eds Sharpton, V. L. & Ward, P. D.) Geological Society of America Special Paper 247, 391–400 (Geological Society of America, 1990). https://doi.org/10.1130/SPE247-p391.

[5] Kaiho, K. *et al.* Global climate change driven by soot at the K-Pg boundary as the cause of the mass extinction. *Sci. Rep.* **6**, 28427 (2016). https://doi.org/10.1038/srep28427.

[6] Bardeen, C. G., Garcia, R. R., Toon, O. B. & Conley, A. J. On transient climate change at the Cretaceous-Paleogene boundary due to atmospheric soot injections. *Proc. Natl Acad. Sci. USA* **114**, E7415–E7424 (2017). https://doi.org/10.1073/pnas.1708980114.

[7] Tabor, C. R., Bardeen, C. G., Otto-Bliesner, B. L., Garcia, R. R. & Toon, O. B. Causes and climatic consequences of the impact winter at the Cretaceous-Paleogene boundary. *Geophys. Res. Lett.* **47**, e60121 (2020). https://doi.org/10.1029/2019GL085572.

[8] Melosh, H. J., Schneider, N. M., Zahnle, K. J. & Latham, D. Ignition of global wildfires at the Cretaceous/Tertiary boundary. *Nature* **343**, 251–254 (1990). https://doi.org/10.1038/343251a0.

[9] Kring, D. A. & Durda, D. D. Trajectories and distribution of material ejected from the Chicxulub impact crater: implications for postimpact wildfires. *J. Geophys. Res. Planets* **107**, 5062 (2002). https://doi.org/10.1029/2001JE001532.

[10] Morgan, J., Artemieva, N. & Goldin, T. Revisiting wildfires at the K-Pg boundary. *J. Geophys. Res. Biogeosci.* **118**, 1508–1520 (2013). https://doi.org/10.1002/2013JG002428.

[11] Goldin, T. J. & Melosh, H. J. Self-shielding of thermal radiation by Chicxulub impact ejecta: firestorm or fizzle? *Geology* **37**, 1135–1138 (2009). https://doi.org/10.1130/G30433A.1.

[12] Johnson, B. C., Johnson, A. V., Wakita, S. & Robertson, D. S. Heat and wildfires during the K-Pg mass extinction enhanced by fine dust. *J. Geophys. Res. Biogeosci.* **131**, e2026JG009837 (2026). https://doi.org/10.1029/2026JG009837.

[13] Belcher, C. M., Collinson, M. E., Sweet, A. R., Hildebrand, A. R. & Scott, A. C. Fireball passes and nothing burns—the role of thermal radiation in the Cretaceous-Tertiary event: evidence from the charcoal record of North America. *Geology* **31**, 1061–1064 (2003). https://doi.org/10.1130/G19989.1.

[14] Belcher, C. M., Collinson, M. E. & Scott, A. C. Constraints on the thermal energy released from the Chicxulub impactor: new evidence from multi-method charcoal analysis. *J. Geol. Soc.* **162**, 591–602 (2005). https://doi.org/10.1144/0016-764904-104.

[15] Harvey, M. C., Brassell, S. C., Belcher, C. M. & Montanari, A. Combustion of fossil organic matter at the Cretaceous-Paleogene (K-P) boundary. *Geology* **36**, 355–358 (2008). https://doi.org/10.1130/G24646A.1.

[16] Belcher, C. M., Finch, P., Collinson, M. E., Scott, A. C. & Grassineau, N. V. Geochemical evidence for combustion of hydrocarbons during the K-T impact event. *Proc. Natl Acad. Sci. USA* **106**, 4112–4117 (2009). https://doi.org/10.

1073/pnas.0813117106.

[17] Robertson, D. S., Lewis, W. M., Sheehan, P. M. & Toon, O. B. K–Pg extinction: Reevaluation of the heat-fire hypothesis. *J. Geophys. Res. Biogeosci.* **118**, 329–336 (2013). https://doi.org/10.1002/jgrg.20018.

[18] Lyons, S. L. *et al.* Organic matter from the Chicxulub crater exacerbated the K-Pg impact winter. *Proc. Natl Acad. Sci. USA* **117**, 25327–25334 (2020). https://doi.org/10.1073/pnas.2004596117.

[19] Morgan, J. V., Bralower, T. J., Brugger, J. & Wünnemann, K. The Chicxulub impact and its environmental consequences. *Nat. Rev. Earth Environ.* **3**, 338–354 (2022). https://doi.org/10.1038/s43017-022-00283-y.

[20] Toon, O. B., Bardeen, C. & Garcia, R. Designing global climate and atmospheric chemistry simulations for 1 and 10 km diameter asteroid impacts using the properties of ejecta from the K-Pg impact. *Atmos. Chem. Phys.* **16**, 13185–13212 (2016). https://doi.org/10.5194/acp-16-13185-2016.

[21] Yu, P. *et al.* Black carbon lofts wildfire smoke high into the stratosphere to form a persistent plume. *Science* **365**, 587–590 (2019). https://doi.org/10.1126/science.aax1748.

[22] Redfern, S. *et al.* Upper troposphere smoke injection from large areal fires. *J. Geophys. Res. Atmos.* **126**, e2020JD034332 (2021). https://doi.org/10.1029/2020JD034332.

[23] Morel, A. Optical modeling of the upper ocean in relation to its biogenous matter content (Case I waters). *J. Geophys. Res. Oceans* **93**, 10749–10768 (1988). https://doi.org/10.1029/JC093iC09p10749.

[24] Pan, Y., Birdsey, R. A., Phillips, O. L. & Jackson, R. B. The structure, distribution, and biomass of the world's forests. *Annu. Rev. Ecol. Evol. Syst.* **44**, 593–622 (2013). https://doi.org/10.1146/annurev-ecolsys-110512-135914.

[25] Arinobu, T., Ishiwatari, R., Kaiho, K. & Lamolda, M. A. Spike of pyrosynthetic polycyclic aromatic hydrocarbons associated with an abrupt decrease in $\delta^{13}$C of a terrestrial biomarker at the Cretaceous-Tertiary boundary at Caravaca, Spain. *Geology* **27**, 723–726 (1999). https://doi.org/10.1130/0091-7613(1999)027⟨0723:SOPPAH⟩2.3.CO;2.

[26] Yu, P. *et al.* Persistent stratospheric warming due to 2019–2020 Australian wildfire smoke. *Geophys. Res. Lett.* **48**, e2021GL092609 (2021). https://doi.org/10.1029/2021GL092609.

[27] Matichuk, R. I., Colarco, P. R., Smith, J. A. & Toon, O. B. Modeling the transport and optical properties of smoke aerosols from African savanna fires during the

Southern African Regional Science Initiative campaign (SAFARI 2000). *J. Geophys. Res. Atmos.* **112**, D08203 (2007). https://doi.org/10.1029/2006JD007528.

[28] Hansen, H. J., Gwozdz, R., Hansen, J. M., Bromley, R. G. & Rasmussen, K. L. The diachronous C/T plankton extinction in the Danish Basin. In *Global Bio-Events: A Critical Approach* (ed. Walliser, O. H.) Lecture Notes in Earth Sciences Vol. 8, 381–384 (Springer, 1986). https://doi.org/10.1007/BFb0010222.

[29] Haq, B. U. Cretaceous eustasy revisited. *Glob. Planet. Change* **113**, 44–58 (2014). https://doi.org/10.1016/j.gloplacha.2013.12.007.

[30] Sewall, J. O. *et al.* Climate model boundary conditions for four Cretaceous time slices. *Clim. Past* **3**, 647–657 (2007). https://doi.org/10.5194/cp-3-647-2007.

[31] Jacobson, M. Z. Correction to "Control of fossil-fuel particulate black carbon and organic matter, possibly the most effective method of slowing global warming". *J. Geophys. Res. Atmos.* **110**, D14105 (2005). https://doi.org/10.1029/2005JD005888.

[32] Danabasoglu, G. *et al.* The Community Earth System Model version 2 (CESM2). *J. Adv. Model. Earth Syst.* **12**, e2019MS001916 (2020). https://doi.org/10.1029/2019MS001916.

[33] Marsh, D. R. *et al.* Climate change from 1850 to 2005 simulated in CESM1 (WACCM). *J. Clim.* **26**, 7372–7391 (2013). https://doi.org/10.1175/JCLI-D-12-00558.1.

[34] Bardeen, C. G., Toon, O. B., Jensen, E. J., Marsh, D. R. & Harvey, V. L. Numerical simulations of the three-dimensional distribution of meteoric dust in the mesosphere and upper stratosphere. *J. Geophys. Res. Atmos.* **113**, D17202 (2008). https://doi.org/10.1029/2007JD009515.

[35] Lawrence, D. M. *et al.* Parameterization improvements and functional and structural advances in version 4 of the Community Land Model. *J. Adv. Model. Earth Syst.* **3**, M03001 (2011). https://doi.org/10.1029/2011MS00045.

[36] Danabasoglu, G. *et al.* The CCSM4 ocean component. *J. Clim.* **25**, 1361–1389 (2012). https://doi.org/10.1175/JCLI-D-11-00091.1.

[37] Long, M. C. *et al.* Simulations with the Marine Biogeochemistry Library (MARBL). *J. Adv. Model. Earth Syst.* **13**, e2021MS002647 (2021). https://doi.org/10.1029/2021MS002647.

[38] Hunke, E. C. & Lipscomb, W. H. *CICE: The Los Alamos Sea Ice Model Documentation and Software User's Manual, Version 4.0.* Tech. Rep. LA-CC-06-012 (Los Alamos National Laboratory, 2008).

[39] Markwick, P. J. & Valdes, P. J. Palaeo-digital elevation models for use as boundary conditions in coupled ocean-atmosphere GCM experiments: a Maastrichtian (late Cretaceous) example. *Palaeogeogr. Palaeoclimatol. Palaeoecol.* **213**, 37–63 (2004). https://doi.org/10.1016/j.palaeo.2004.06.015.

[40] Milligan, J. N., Royer, D. L., Franks, P. J., Upchurch, G. R. & McKee, M. L. No evidence for a large atmospheric $CO_2$ spike across the Cretaceous-Paleogene boundary. *Geophys. Res. Lett.* **46**, 3462–3472 (2019). https://doi.org/10.1029/2018GL081215.

[41] Beerling, D. J., Lomas, M. R. & Gröcke, D. R. On the nature of methane gas-hydrate dissociation during the Toarcian and Aptian oceanic anoxic events. *Am. J. Sci.* **302**, 28–49 (2002). https://doi.org/10.2475/ajs.302.1.28.

[42] Gough, D. O. Solar interior structure and luminosity variations. In *Physics of Solar Variations* (ed. Domingo, V.) 21–34 (Springer, 1981). https://doi.org/10.1007/978-94-010-9633-1_4.

[43] Reid, J. S., Koppmann, R., Eck, T. F. & Eleuterio, D. P. A review of biomass burning emissions part II: intensive physical properties of biomass burning particles. *Atmos. Chem. Phys.* **5**, 799–825 (2005). https://doi.org/10.5194/acp-5-799-2005.

[44] Wolbach, W. S., Lewis, R. S. & Anders, E. Cretaceous extinctions: evidence for wildfires and search for meteoritic material. *Science* **230**, 167–170 (1985). https://doi.org/10.1126/science.230.4722.167.

[45] During, M. A. D. *et al.* The Mesozoic terminated in boreal spring. *Nature* **603**, 91–94 (2022). https://doi.org/10.1038/s41586-022-04446-1.

[46] DePalma, R. A. *et al.* Seasonal calibration of the end-Cretaceous Chicxulub impact event. *Sci. Rep.* **11**, 23704 (2021). https://doi.org/10.1038/s41598-021-03232-9.

[47] Wolfe, J. A. Palaeobotanical evidence for a June 'impact winter' at the Cretaceous/Tertiary boundary. *Nature* **352**, 420–423 (1991). https://doi.org/10.1038/352420a0.

[48] Wolbach, W. S., Gilmour, I., Anders, E., Orth, C. J. & Brooks, R. R. Global fire at the Cretaceous-Tertiary boundary. *Nature* **334**, 665–669 (1988). https://doi.org/10.1038/334665a0.

[49] Kalashnikova, O., Horányi, M., Thomas, G. E. & Toon, O. B. Meteoric smoke production in the atmosphere. *Geophys. Res. Lett.* **27**, 3293–3296 (2000). https://doi.org/10.1029/1999GL011338.

[50] Wolbach, W. S., Widicus, S. & Kyte, F. T. A search for soot from global wildfires in central Pacific Cretaceous-Tertiary boundary and other extinction and impact horizon sediments. *Astrobiology* **3**, 91–97 (2003). https://doi.org/10.1089/

153110703321632444.

## Acknowledgements

We acknowledge the computing and storage resources provided by the Computational and Information Systems Laboratory (CISL) at NCAR. Model simulations were performed on the NSF National Center for Atmospheric Research Cheyenne supercomputer (https://doi.org/10.5065/D6RX99HX) and the Derecho supercomputer (https://doi.org/10.5065/qx9a-pg09).

## Funding

C.R.T. acknowledges funding from NSF award 2021686. J.C., N.S.L., and J.S. acknowledge funding from NSF award 2021648. K.G.M acknowledges funding from NSF award 2021262. C.H acknowledges funding from NSF award 2149890. S.M acknowledges funding from NSF award 2020380 Funding for this work was also provided by the Future of Life Institute. This material is based upon work supported by the National Center for Atmospheric Research, which is sponsored by the NSF under Cooperative Agreement 1852977.

## Author contributions

O.B.T., S.H., C.B., and C.R.T. discussed the hypothesis. S.H., C.B., and C.R.T. participated in the model development. S.H. performed the model simulation and analyzed the model-proxy comparison. W.S.W advised on the evaluation and interpretation of the sedimentation records. All the authors wrote and edited the manuscript.

## Competing interests

The authors declare no competing interests.

## Supplementary Files

This is a list of supplementary files associated with this preprint. Click to download.

- SupportingInformationHu.pdf